Three-Dimensional Hydrodynamics Associated with a Solitary Wave Traveling over an Alongshore Variable Shallow Shelf

Patrick J. Lynett, M.ASCE[1]; David Swigler[2]; Hoda El Safty[3]; Luis Montoya[4]; Adam S. Keen, S.M.ASCE[5]; Sangyoung Son[6]; and Pablo Higuera[7]

Abstract: We investigated, from two laboratory experiments, the kinematic behavior and the three-dimensional turbulence that is generated due to a breaking solitary wave propagating over irregular shallow water bathymetry. The bathymetry was composed of a deep water region followed by a shallow shelf via a relatively steep slope. The offshore boundary of the shelf break varied in the longshore direction. The shelf had a triangular shape in plan view, with the widest part of the shelf located along the center of the basin. The first experiment used a planar shelf, while an obstacle in the shape of a conical island was placed near the shelf apex for the second experiment. Measurements of fluid velocities and free surface elevations were collected using three-dimensional acoustic Doppler velocimeters (ADVs) and wave gauges, respectively. In the first experiment, the inundating flow varied weakly in the alongshore direction, but demonstrated strong variations in the second experiment. A refraction-generated jetting mechanism caused by the convergence of water mass near the basin centerline characterized the run-up. The greatest cross-shore velocities were located near the basin's centerline and were triggered by the jetting mechanism. The greatest turbulent events were well correlated with four identified bore fronts. The bore fronts were generated by a combination of waves including the leading wave, beach reflections, and shelf oscillations. A primary conclusion of this study is that nonlinear long-wave transformation over irregular bathymetry can lead to a highly complex nearshore wave field with little apparent correlation to the offshore wave. **DOI: 10.1061/(ASCE)WW.1943-5460.0000525.**

Introduction

It is important to study and understand the kinematic properties and turbulent energy associated with a breaking wave when trying to predict wave forces on structures, sediment transport, nearshore mixing, circulations, and ultimately coastal morphology. There have been comprehensive experimental and numerical studies focused on advancing the understanding of turbulence that develops as waves interact with an underlying bathymetry. These studies have largely focused on mean flows that are two-dimensional. The goal of this study is to better understand the kinematic properties and three-dimensional turbulence that develops as a solitary wave evolves over an irregular bathymetry.

Numerous experimental studies have been conducted to develop our understanding of the physics that govern the evolution of waves as they approach a shoreline. These experiments have increased our understanding of wave mechanisms related to shoaling, refraction, breaking, and turbulence generation and dissipation. While not a proper physical analogy to tsunamis (e.g., Madsen et al. 2008), solitary waves are often utilized to understand the behavior of transient long waves in shallow water. Such solitary wave experiments are then used, among other purposes, to validate and benchmark long-wave numerical models, which might then be applied to geophysical-scale tsunami simulations with some increased level of confidence.

Previous solitary wave experiments measured the run-up on plain beaches (e.g., Synolakis 1987; Gedik et al. 2005; Hsiao et al. 2008), vertical walls (e.g., Liu and Al-Banaa 2004), piecewise linear beaches (e.g., Monaghan and Kos 1999), and around idealized islands or spatially variable topography (e.g., Liu et al. 1995). The wealth of experimental run-up data utilizing solitary waves is large, and these data have experienced widespread use in model validation (e.g., Liu et al. 1991). Solitary wave experiments have been employed in a more limited manner for coastal transformation (e.g., Grilli et al. 1994b). Existing velocity measurements under solitary waves are less common, which then leads to a modeling deficiency; for example, long-wave models not specifically validated for velocity should not be used as predictors of velocity-governed processes, such as transport and fluid drag.

Experimental wave breaking studies often focus on turbulence

[1]Professor, Dept. of Civil Engineering, Univ. of Southern California, Los Angeles, CA 90254 (corresponding author). ORCID: https://orcid.org/0000-0002-2856-9405. Email: plynett@usc.edu

[2]Coastal Engineer, Coastal Planning & Engineering, 2505 NW Everglades Blvd., Stuart, FL 34994; formerly Graduate Student, Dept. of Civil Engineering, Texas A&M Univ., College Station, TX 77840. Email: daveswigler@gmail.com

[3]Assistant Professor, Irrigation and Hydraulics Dept., Faculty of Engineering, Cairo Univ., P.O. Box 12211, Giza 12613, Egypt; formerly Researcher, Dept. of Civil Engineering, Univ. of Southern California, Los Angeles, CA 90254. Email: hodael_safty@yahoo.com

[4]Graduate Student, Dept. of Civil Engineering, Univ. of Southern California, Los Angeles, CA 90254. ORCID: https://orcid.org/0000-0002-3285-1964. Email: lhmontoy@usc.edu

[5]Graduate Student, Dept. of Civil Engineering, Univ. of Southern California, Los Angeles, CA 90254. ORCID: https://orcid.org/0000-0002-8236-0848. Email: adamkeen@usc.edu

[6]Associate Professor, School of Civil, Environmental and Architectural Engineering, Korea Univ., Seoul 02841, South Korea. ORCID: https://orcid.org/0000-0002-2819-5140. Email: sson@korea.ac.kr

[7]Researcher, Dept. of Civil and Environmental Engineering, National Univ. of Singapore, Singapore 119077. ORCID: https://orcid.org/0000-0003-2233-360X. Email: pablo.higuera@nus.edu.sg

Note. This manuscript was submitted on May 21, 2018; approved on February 11, 2019; published online on September 11, 2019. Discussion period open until February 11, 2020; separate discussions must be submitted for individual papers. This paper is part of the ***Journal of Waterway, Port, Coastal, and Ocean Engineering***, © ASCE, ISSN 0733-950X.

generation and evolution. For example, Lin and Hwung (1992) examined the leading jet of a breaking wave and hypothesized a mechanism for air entrapment by breaking waves. As the flow transitions from irrotational to rotational motion, the entrained air along with the violent impact of the jet causes significant turbulence to develop within the water column (Grilli et al. 1994a). Studies have noted that the turbulence under a plunging breaker is greater than that under a spilling breaker and greatly depends on both the deep-water-wave conditions and beach slope. The turbulent energy is dissipated within one wave cycle and transported landward by the mean flow under a plunging breaker, while under a spilling breaker the turbulent energy is dissipated at a much slower rate and transported seaward (Ting and Kirby 1994, 1995). Relevant to the solitary wave processes to be discussed in this paper, Ting (2006) performed a detailed study of the turbulence under a breaking solitary wave. While his experiments focused on a one-horizontal-dimension bathymetry and incident wave, he was able to observe and quantify the turbulence throughout the water column and along the depth profile. Here, we aim for a similar type of measurement across a larger area including two-horizontal-dimension evolution, albeit with a significantly coarser spatial resolution.

The objective of our laboratory experiment was to provide fundamental hydrodynamic information that can be used to increase understanding of long waves as they approach a shoreline. This study presents the characteristics of a breaking solitary wave (1) over an irregular, three-dimensional bathymetry; and (2) over an irregular, three-dimensional bathymetry with a conical island. The following sections describe the basin and instrument layouts used in the experiments along with the laboratory procedures, followed by details of the free surface elevation, flow velocity, and turbulence measurements. The evolution of a single solitary wave, its run-up on a planar beach, and the resulting hydrodynamic and turbulence characteristics over a complex shallow water shelf and around the conical island are discussed with the use of visual observations, wave gauge measurements, and acoustic Doppler velocimeter (ADV) velocity measurements. Differences between the two experiments are provided. Some of the laboratory details presented in this paper have been previously discussed in Lynett et al. (2011), and herein we provide a significantly expanded presentation of the experimental effort.

Experiment Setup and Procedure

Basin Layout

Laboratory experiments were performed to better understand the kinematic properties and turbulence associated with a breaking solitary wave. These experiments were conducted with a large number of spatially distributed free surface elevation and fluid velocity measurements. The experiments took place in the Tsunami Wave Basin at Oregon State University. This basin is 48.8 m long and 26.5 m wide, equipped with a large-stroke, piston-type wavemaker, which for the experiments discussed herein generated a single solitary wave. At the wavemaker, the water depth was 78 cm and the target height for the generated solitary wave was 39 cm for all the trials discussed in this paper. The underlying basin bathymetry and the tank sidewalls were made of smooth concrete. Fig. 1 presents the coordinate system adopted in this study, with $X = 0$ located at the wavemaker and increasing across the length of the basin; $Y = 0$ located at the centerline of the basin with positive oriented parallel to the wavemaker to agree with the right-hand rule; and $Z = 0$ located at the basin floor in the constant-depth portion of the basin near the wavemaker with positive directed upward.

A concrete shelf beach bathymetry was built for the two experiment sets, whose cross section is shown in Fig. 1. This bathymetry forced the generated solitary wave to break symmetrically about the centerline of the basin ($Y = 0$ m). A three-dimensional shelf was built from $X = 10.2$ m extending to $X = 25.5$ m. The shelf was triangular shaped (in plan view), with the apex of the triangle closest to the wavemaker and a 1:30-slope planar beach at the shoreward side. The elevation at the offshore shelf edge was $Z = 0.71$ m, with the apex located at $X = 12.6$ m. There was a

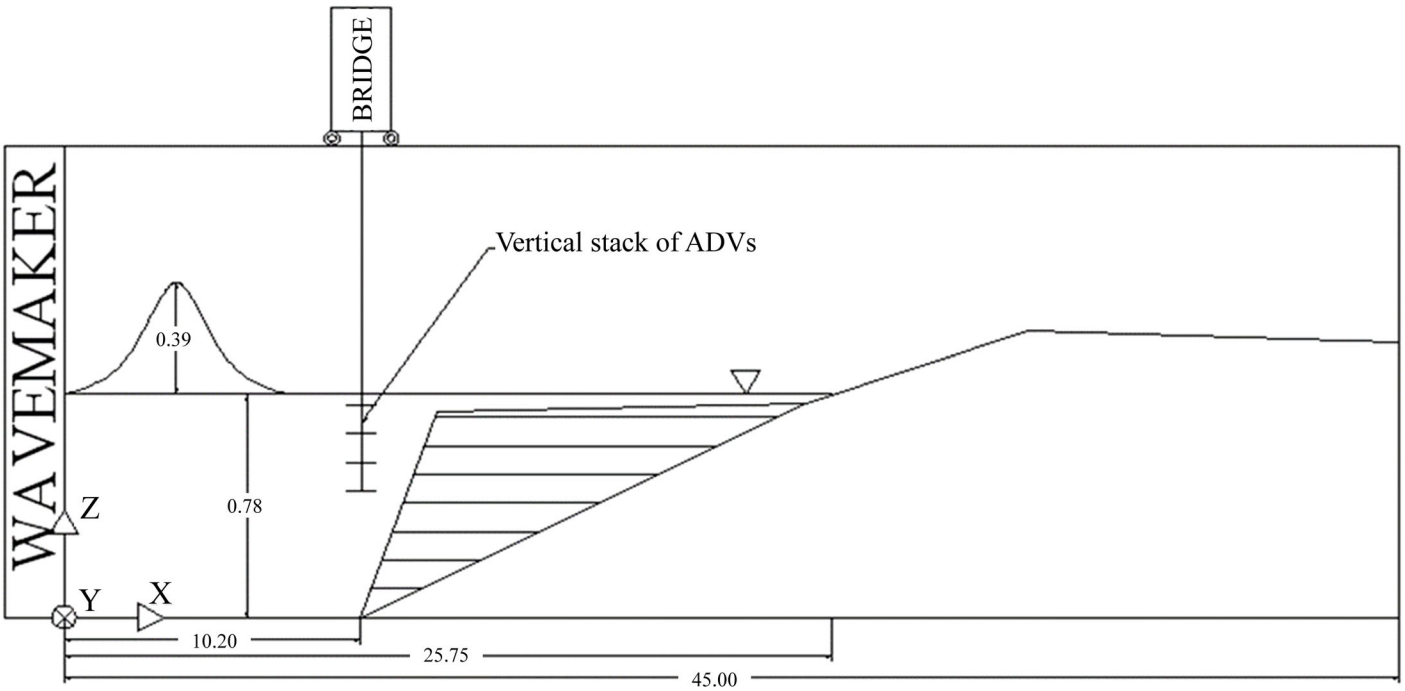

Fig. 1. Elevation view of first experiment setup. All dimensions are in meters.

J. Waterway, Port, Coastal, Ocean Eng., 2019, 145(6): 04019024

variation in the slope of the shelf break, with the steepest slope at the apex, then becoming milder from the shelf edge to the basin side walls. The planar beach continued to $X = 31$ m; after this point, it became nearly horizontal and extended to the back of the basin's wall; there is a slight negative slope in this back section as shown in Fig. 1. The still-water shoreline (SWS) intersected the planar beach at $X = 25.75$ m and the water level was maintained at an elevation of 0.78 m ($Z = 0.78$ m). For the second experiment, a conical island was built landward of the shelf apex. The island center was located at $X = 17.0$ m, with a base radius of 3.0 m and peak height of 0.45 m above the still-water depth. A three-dimensional view of the basin with the conical island is shown in Fig. 2.

Instrument Layouts

Various instruments were used to record the free surface elevations and fluid velocities associated with the solitary wave. To measure the free surface elevation, resistance and acoustic wave gauges were used. ADVs were employed to capture fluid velocities. A data acquisition system (DAQ) recorded the measurements from the instruments at a sampling frequency of 50 Hz. Instruments were mounted either to the bottom of the basin with brackets or to a moveable bridge aligned in the alongshore direction. The bridge was positioned at various cross-shore locations. Only a small fraction of the total set of measurement locations were included in each of the many trials, reducing the impacts to the flow due to instrumentation interference and at the same time providing a detailed representation of the dynamics experienced during the experiments.

Wave Gauges

Free surface elevation was measured using two types of wave gauges. These measurements allowed the evolution of the solitary wave over the shelf, around the island, and up the beach to be tracked and quantified. During the experiment, water depth was varied off shore and on shore. This constrained the measurements to two types of wave gauges: (1) resistance-type, wire wave gauges (rWGs), used off shore and on the shelf; and (2) ultrasonic wave gauges (usWGs), used on shore of SWS.

For each experiment, a total of 14 rWGs were used and attached to the bridge. In the first experiment set, the rWGs were positioned from $Y = -12$ m to $Y = 12$ m with 1-m spacing on the bridge in the longshore direction. Then the bridge was positioned at the following cross-shore locations: $X = 5$, 7.5, 9, 11.5, 13, 15, 17, 19, 21, 23, and 25 m. There were a total of 275 different rWG locations throughout the basin as shown by white asterisks in Fig. 3. The usWGs were used to track the propagation of the breaking solitary wave up and down the planar beach. Five usWGs were used and were located on the bridge at $Y = 0$, 2, 5, 7, and 10 m and were then positioned at X= 23, 25, 27, 29, 31, 33, 35, 37, and 39 m. To colocate the two types of instruments and test the consistency of the recorded free surface time series, the first two bridge locations of the usWG layout were the same as the last two bridge locations of the rWG layouts. There were a total of 45 usWG locations throughout the basin as shown by the black diamonds in Fig. 3. For the second experiment, the wave gauges were positioned at a similar set of locations throughout the basin. Differences in measurement locations between the two experiments were due to the placement of the island. Overall, however, the coverage and type of measurements were consistent between the no-island and with-island experiments.

Acoustic Doppler Velocimeters

Nortek Vectrino 3D ADVs (Nortek, Rud, Norway) were used to measure the three components of fluid velocities (U, V, and W) simultaneously. Two vertical stacks of four ADVs (eight total) were

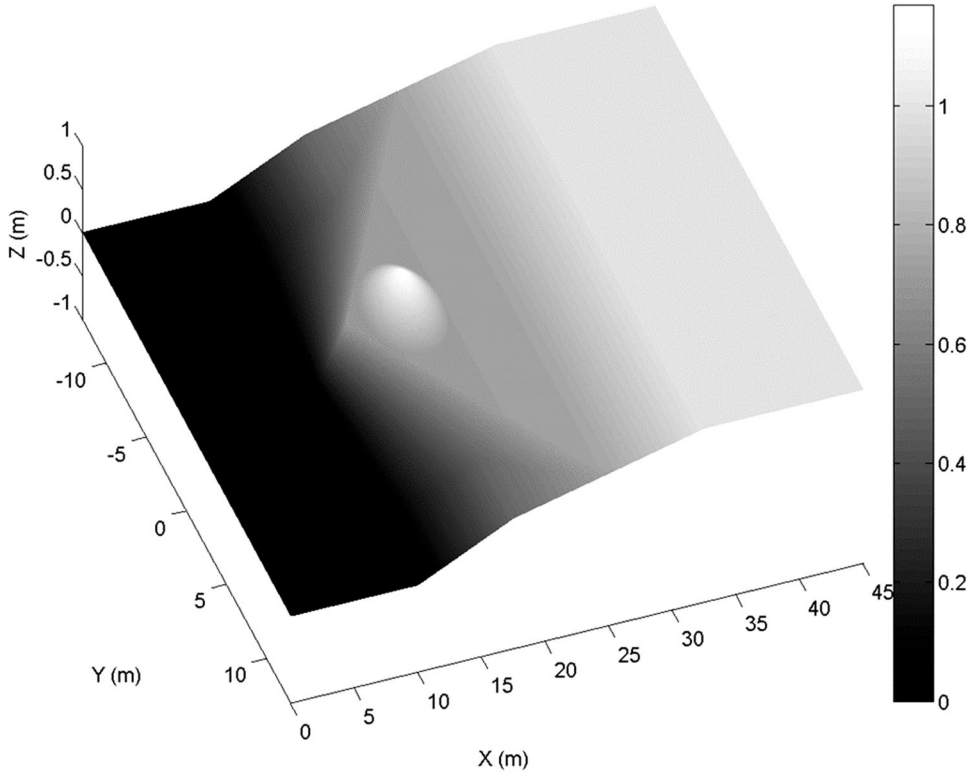

Fig. 2. Three-dimensional view of second, with-island, experiment bathymetry. All dimensions are in meters.

J. Waterway, Port, Coastal, Ocean Eng., 2019, 145(6): 04019024

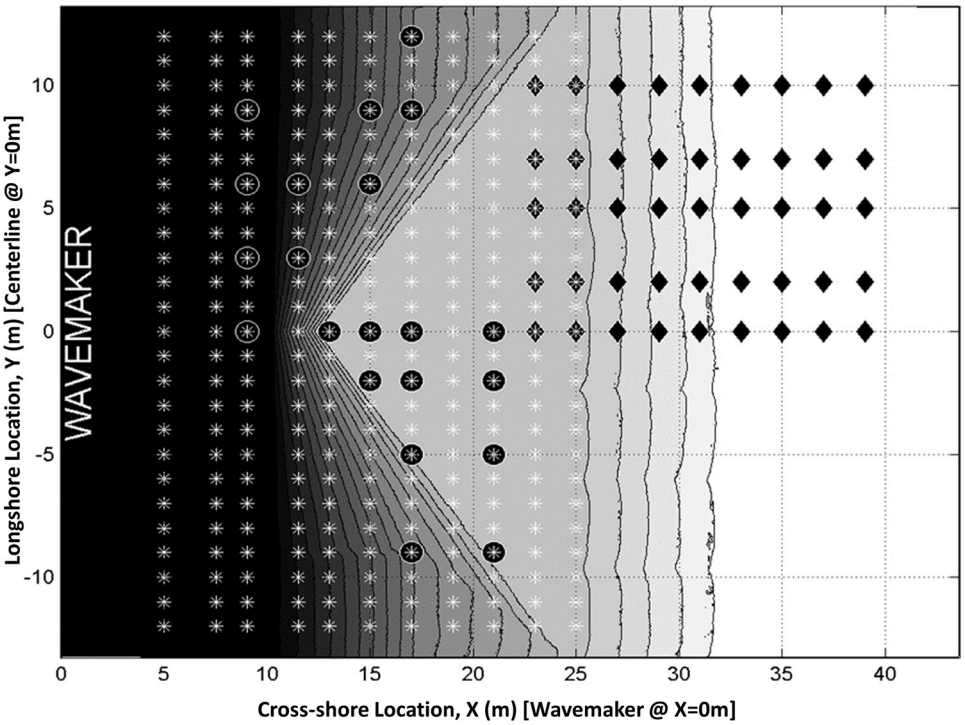

Fig. 3. ADV (black circles), rWG (asterisks), and usWG (black diamonds) instrument location plan with bathymetry for the experiments. The layout for the first (no-island) experiment is shown here; the layout for the second (with-island) experiment is similar, with modification to account for the island.

mounted to the bridge to obtain a vertical flow profile as shown in Fig. 1. On the stacks, the uppermost submerged ADV was 5 cm below the still-water surface and the ADVs were spaced 10 cm apart in the vertical direction. The vertical stacks were positioned such that the bottommost ADV was as close to the bathymetry surface as possible. The other (nonstacked) ADVs were located at the bathymetry surface on or near the shelf. For the first experiment, the ADVs were deployed in multiple configurations, yielding a total of 51 locations throughout the basin and 80 locations for the second experiment. The ADVs are shown by black circles in Fig. 3, with the bottom-mounted instruments located at $X \geq 13$ m and $Y \leq 0$ m. The remaining locations shown in Fig. 3 are the bridge-mounted vertical stacks of ADVs.

Procedure

The wave heights and fluid velocity measurements were often colocated, but were performed separately in order to minimize instrumental flow interference. For each type of measurement device, multiple trials were conducted to ensure the consistency of the data. A trial consisted of generating a single wave with the wavemaker and recording data for approximately 2 min. Based on observations of surface tracers, the basin was allowed to calm for 35 min in between trials, when residual currents would diminish to less than 0.1 cm/s.

For both wave gauges (rWGs and usWGs), two trials were run at each location to confirm the repeatability of the waves generated by the wavemaker and to confirm the consistency of the recorded time series. For a reasonable quantification of the mean flow and turbulent fluctuations measured by the ADVs, a minimum of 20 trials for each location were performed. The data set presented herein was generated from more than 500 individual trials, all using the same depth and wave conditions.

Measurements

Repeatability

The rWG time series closest to the wavemaker ($X = 5$ m, various Y) were analyzed to confirm the repeatability of the generated solitary wave. In total, measurements from 28 different trials were compared, as shown in Fig. 4. The analysis indicated that wave heights ranged from 0.363 to 0.373 m, with a mean and standard deviation of 0.368 and 0.002 m, respectively. This result confirms the repeatability of the generated solitary wave. Also shown in Fig. 4 is the solitary wave solution provided by a high-order Boussinesq-type model (Lynett and Liu 2004). Comparison between the experimental and numerical solutions indicates that the experimental wave is not perfectly symmetrical but does provide a shape very close to the idealized analytic (numerical) solution. In particular, the trailing trough is a likely relic of the experimental difficulty of generating a solitary wave of this high nonlinearity; however, this trough shape is still repeatable. A reasonable conclusion of this comparison is that if one was to compare the experimental data presented in this paper with a high-resolution numerical model that, for example, resolves turbulence properties, the incident wave should preferably be generated with the wavemaker trajectory (shown in the inset of Fig. 4) and not an idealized solitary wave solution.

The free surface elevation time series obtained from rWG locations in symmetrical locations on opposite sides of the centerline at all X locations were found to confirm the symmetry of the wave as it evolved through the basin. While not shown here, the symmetry of the waveform throughout the basin showed a consistency equal to that found in the previous repeatability analysis. The remainder of the paper will focus on the bottom half of the basin ($Y < 0$ m) because the on-shelf ADV locations were concentrated in this half. Aspects of the flow will be described through the following data relationships:

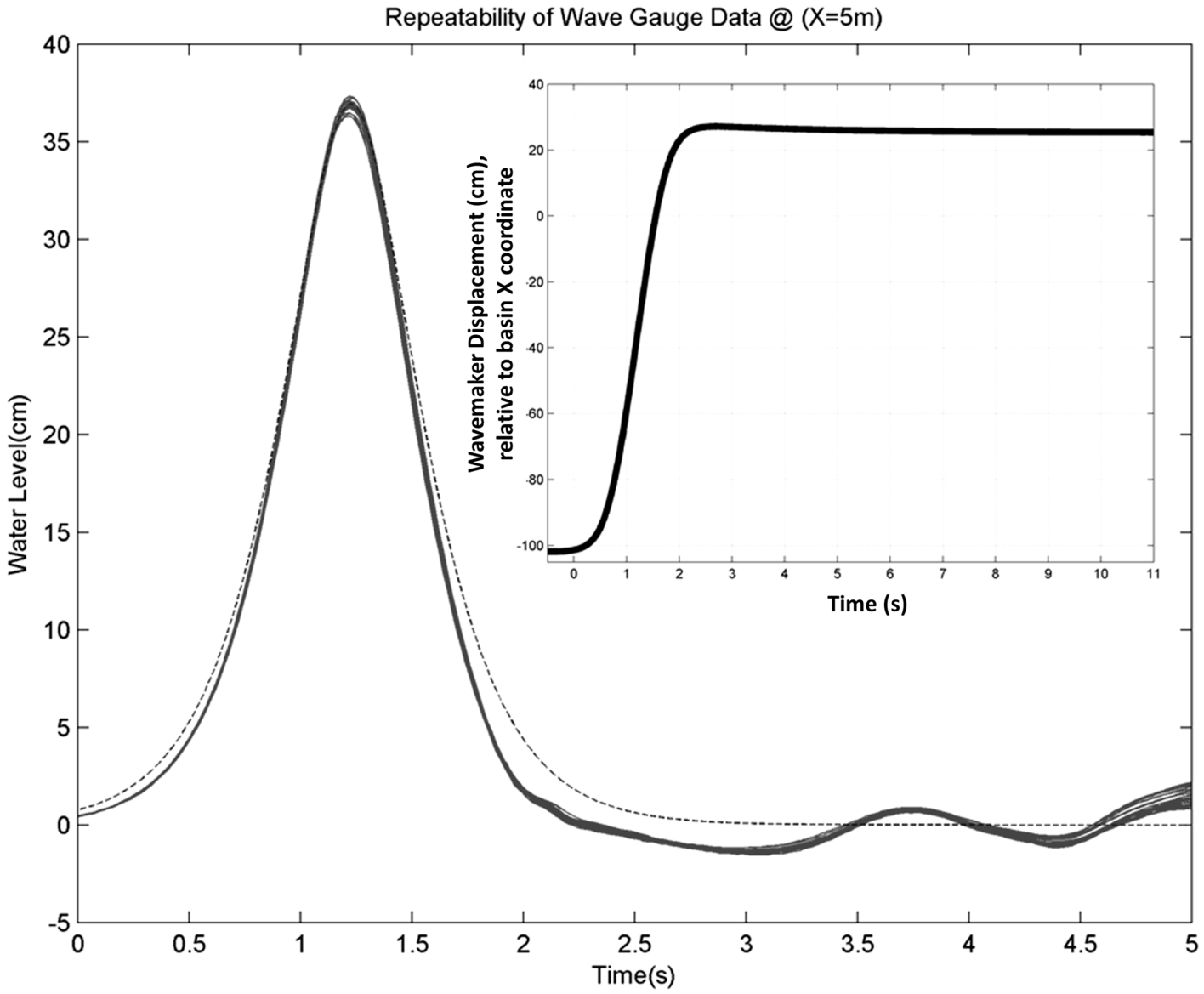

Fig. 4. rWG repeatability from long rWG located at $X = 5$ m. Twenty-eight experimental time series are given by the solid lines, and the numerical result from the model of Lynett and Liu (2004) is given by the dashed line. In the inset, the wavemaker trajectory time series is given by the black line.

rWGs describing the free surface offshore of the SWS, usWGs describing the run-up shoreward of the SWS, the bridge-mounted ADVs describing the flow off shore of the shelf edge, and the bottom-mounted ADVs describing the flow on shore of the shelf edge.

Turbulence Calculations

Multiple trials were run to obtain a set of instantaneous velocity (U, V, and W) time series that could be analyzed to estimate turbulence quantities. After collecting at least 20 trials, erroneous segments in each velocity time series that result from aeration and instrument emergence were removed from the trial. The trials were then ensemble-averaged to evaluate the mean flow time series ($\overline{U}$, $\overline{V}$, and $\overline{W}$) at the ADV location. Instantaneous turbulent velocity fluctuations for each trial (u', v', and w') were determined by subtracting the mean flow time series from the instantaneous time series. Once the instantaneous turbulent velocity time series were obtained, Reynolds stresses could be estimated using methodologies such as those provided in Ting (2006). The average Reynolds stresses ($\overline{u'u'}$, $\overline{v'v'}$, $\overline{w'w'}$, $\overline{u'v'}$, $\overline{u'w'}$, and $\overline{v'w'}$) were quantified by multiplying combinations of instantaneous turbulent velocities. These times series combinations were then ensemble-averaged to obtain time series of Reynolds stresses. Using the Reynolds stresses, the total turbulent kinetic energy (K) is defined as

$$K(t) = \frac{\overline{u'u'} + \overline{v'v'} + \overline{w'w'}}{2}$$

Observed Wave Evolution

Each solitary wave trial produced complex yet repeatable flow patterns within the basin. These patterns arise out of the flow interaction with the bathymetry and conical island that produce multiple bore fronts and reflected waves. A conceptual understanding of the hydrodynamics in the basin is needed to further discuss the complexity of the free surface elevation, fluid velocity, and turbulent energy. This information can be explained with assistance from video recorded during the trials. In the following section we will discuss the observed wave evolution for the two experiments. An analysis of the

planar shelf experiment will be discussed first. This will be followed by an analysis of the shelf with the conical island.

Triangular-Shaped Shelf

Visually Observed Hydrodynamics

Multiple plan view images of the bottom half of the basin ($Y < 0$ m) are shown in Fig. 5. The images illustrate how wave features develop and evolve in the basin and will help the reader to interpret the data for the remainder of this paper. In the images, the wave propagates from left to right (in the cross-shore direction). Near the top of the images, the basin centerline ($Y = 0$ m) passes thorough the apex of the shelf. The wavemaker is located to the left in the images and the side wall of the basin is located along the bottom (both outside of the field of view). Dye from a visualization study can also been seen near the bottom of some images. For the dye study, dye was released continuously from a point source at the edge of the shelf.

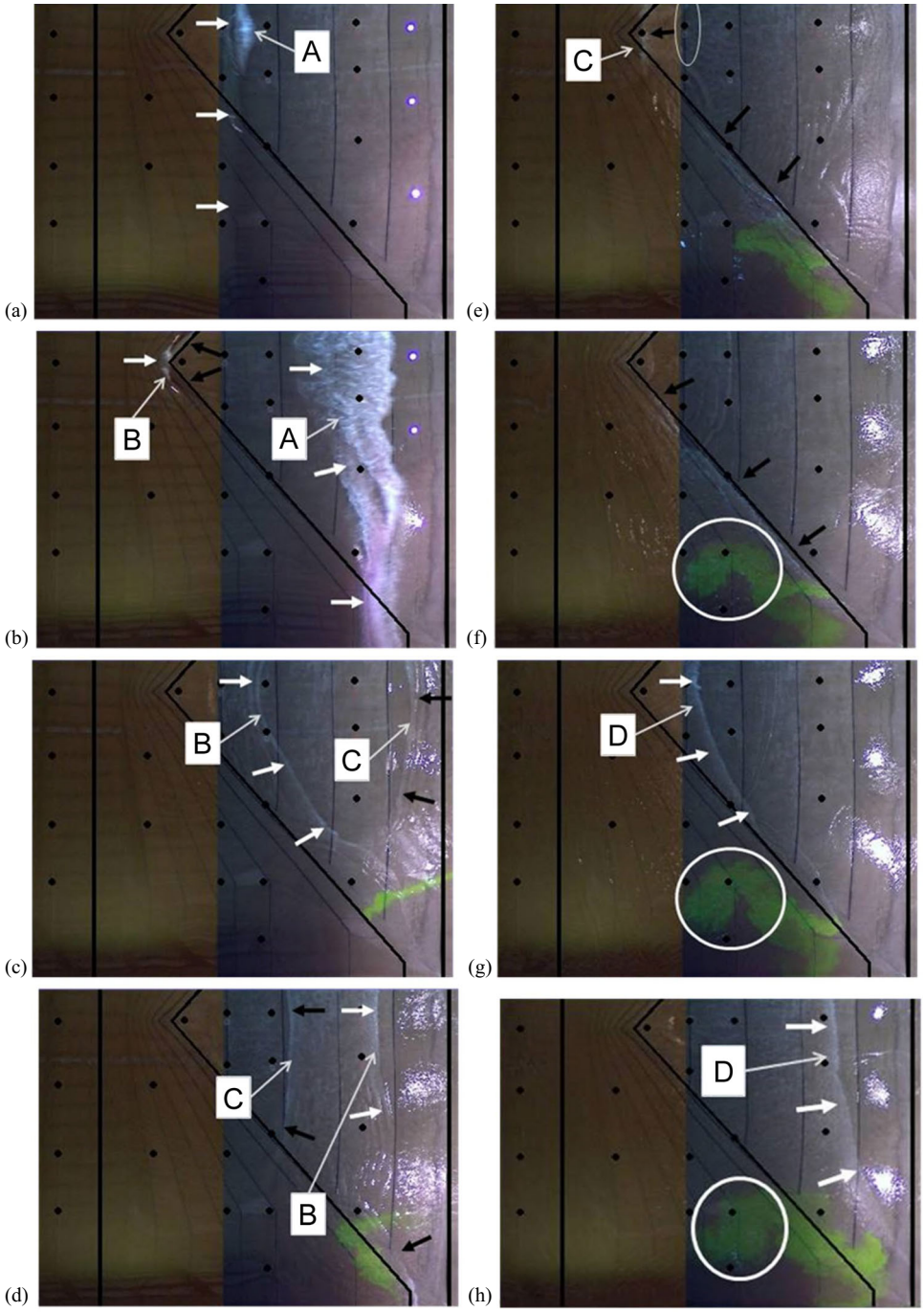

Fig. 5. Basin at (a) 6.2 s; (b) 8.3 s; (c) 16.1 s; (d) 22.1 s; (e) 26.4 s; (f) 31.9 s; (g) 36.9 s; and (h) 41.9 s after the solitary wave was generated. Black circles indicate ADV locations; and arrows indicate mean flow direction, with white arrows indicating onshore flows and black arrows indicating offshore flows. The vertical black line on the left side of the images indicates the end of the constant-depth portion of the tank and the offshore limit of the shelf break, while the vertical black line on the right gives the start of the planar beach. The V-shaped diagonal black lines delineate the edge of the flat portion of the shallow water shelf, or the shelf edge.

J. Waterway, Port, Coastal, Ocean Eng., 2019, 145(6): 04019024

Images in Fig. 5 are arranged in time. Time zero corresponds with the wavemaker activation, just before the paddle moves. Fig. 5(a) corresponds to the solitary wave arriving at the apex of the shelf edge. At this time ($t = 6.2$ s), the wave begins to break just on shore of the shelf apex along the centerline of the basin. The impact of the overturning jet with the free surface (sometimes referred to as a plunging breaker) and resultant mixing can be identified in the image by the localized area of white water. This time also corresponds to the initial development of the bore front labeled Bore Front A. In the images, the white arrows denote the onshore-directed flow associated with Bore Front A.

Fig. 5(b) ($t = 8.3$ s) indicates that the breaking of Bore Front A has spread to the sidewall of the basin. The flow behind Bore Front A is onshore-directed (white arrows), consistent with the direction of wave propagation. Just landward of the apex on top of the shelf, however, the flow is weakly offshore-directed (black arrows). At the apex, the flow is onshore-directed, which is the result of a shelf-generated secondary wave. This wave is labeled as Bore Front B. The physical explanation for Bore Front B is analogous to relaxing flow over a sill. The hydraulic jump near the lee of the sill will propagate as a free wave over and away from the sill once the current decreases. This generation mechanism will be referenced in this paper as a sill-type generation mechanism. The apex of the shelf became dry for a short period of time before the arrival of Bore Front B. This time also corresponds to the start of dye being injected. The injection point is near the bottom of the image but is not visible in the image. Advection of the dye landward with Bore Front A can be seen in Fig. 5(c).

Fig. 5(c) shows Bore Front B propagating shoreward over the shelf and the onshore-directed flow associated with the bore front. Also, visible further on shore in the image is Bore Front C. Bore Front C is a part of Bore Front A that was reflected off SWS. Fig. 5(d) also shows these bore fronts but 4 s later, after they have passed one another. In this image, dye is visible along the edge of the shelf near the basin side wall. The dye is directed off shore following Bore Front C. Six seconds later in Fig. 5(e), Bore Front C converges at the apex of the shelf, while Bore Front B has traveled outside of the field of view. The wave convergence is a result of refraction, where offshore-directed wave energy turns toward the apex and propagates along the shelf edge. In the image, visible dye is being transported off shore, indicating a strong offshore flow. Bore Front C converges at the apex and breaks. The event can clearly be identified in the data as a turbulence event and will be discussed subsequently. The offshore flow along the shelf edge also causes a stationary hydraulic jump to form.

At 31.9 s [Fig. 5(f)], the bore fronts have moved out of the field of view. The hydraulic jump persists due to the strong offshore currents following Bore Front C. The instabilities in this high mixing region eventually shed a large, predictable (repeatable), counterclockwise-rotating eddy. The counterclockwise-rotating eddy is visible as a concentrated area of dye inside the white circle. The eddy (white circle) is still clearly visible 5 s later [Fig. 5(g)]. By this time another wave, labeled Bore Front D, arrives on the shelf traveling on shore. Bore Front D is primarily a sill-type wave resulting from Bore Front C's offshore flow, but also due to the reflection of Bore Front C from the wavemaker. Offshore flow continues on the shelf, but following Bore Front D the flow turns on shore. Bore Front D is near parabolic in its alongshore curvature, similar to Bore Front B. By 41.9 s [Fig. 5(h)], Bore Front D propagates further landward, causing the flow over the shelf to be directed on shore. Even after the flow has changed directions, the eddy remains in the images. The eddy is identifiable as a collection of dye.

Free Surface Displacement

With the descriptions of the wave development discussed in the previous section, free surface displacement measured by the rWG can be analyzed in greater detail. Maximum free surface elevations are shown in Fig. 6. These measurements coincide with the leading solitary wave, described in the previous section as Bore Front A

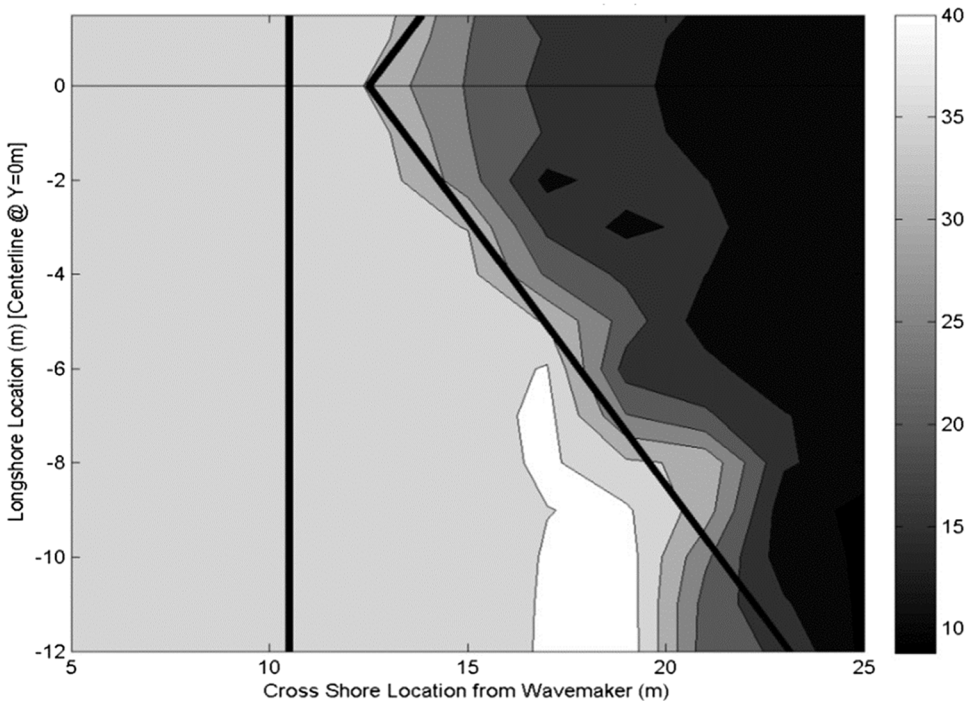

Fig. 6. rWG maximum free surface elevation (cm). The straight black line near $X = 10.2$ m marks the landward end of the constant-depth portion of the basin, while the diagonal black line represents the edge of the triangular shallow water shelf.

J. Waterway, Port, Coastal, Ocean Eng., 2019, 145(6): 04019024

located on the shelf. Off shore from the shelf, the wave height is uniform. Fig. 5 showed Bore Front A starting to break at the apex, with breaking spreading along the shelf edge laterally. The area just off shore of the shelf near the sidewall of the basin is particularly interesting. In this region the wave reaches a maximum height because of shoaling. Since this region also has the mildest offshore slope, we can conclude for this experiment that for milder slopes, shoaling has a greater effect on the wave height.

The bore fronts described in Fig. 5 can be analyzed more easily by first understanding the evolution of the solitary wave from generation to the eventual wave height decay on the shelf. Recordings of free surface elevations from multiple rWG located along the tank centerline are shown in Fig. 7. The figure also labels the four bore fronts discussed in Fig. 5. The bore front propagation direction can be identified by observing the slope of the line that connects the bore crests in each subplot. A positive slope coincides with an offshore-directed bore front, while a negative slope coincides with the onshore-directed bore front.

Fig. 7 shows the solitary wave as it travels across the constant-depth region of the tank at two offshore locations corresponding to $X = 7.5$ and 11.5 m. As Bore Front A moves on shore at $X = 13.0$ m, the front face steepens rapidly. Wave breaking and wave height decay begin once Bore Front A reaches $X = 15.0$ m. However, the plunging breaker jet impacts the free surface shoreward from this location. At $X = 17.0$ and 21.0 m, Bore Front A has traveled on shore and the breaking has caused the wave height to reduce significantly. The crossing of the gray lines at $X = 17.0$ and 21.0 m corresponds to Bore Front B propagating on shore and passing through Bore Front C. As Bore Front C travels off shore and converges with the apex of the shelf due to refraction (at $X = 13.0$ m), the height of Bore Front C increases [described in Fig. 5(e)]. The event (indicated by black arrow) at $X = 15.0$ m is a consequence of the refraction and convergence and results in localized breaking. Bore Front D only propagated onto the shelf after the offshore-directed flow associated with Bore Front C had subsided.

Turbulence Characteristics on Shelf

The components of the mean flow, the associated turbulent fluctuations, and K at the shelf apex are shown in Fig. 8. The data illustrate the relationship between the mean flow and the turbulence. The flow depth remained sufficiently deep to keep the ADV submerged at all times and the incident solitary wave had not begun to break, which resulted in a complete ADV time series. In Figs. 8(a–c), the mean flow, $\overline{U}$, is clearly and expectedly dominant, with a peak magnitude of approximately 2 m/s under the wave crest. The $\overline{V}$ component of the flow is small since the measurement was taken along the centerline of a symmetrical experiment. The vertical component of the mean flow, $\overline{W}$, indicates a small upward-directed (positive) velocity that is associated with the rising crest from the incident solitary wave. This is followed by a downward-directed (negative) velocity. This vertical component of the mean flow is inconsistent with potential flow theory. The result suggests that bottom shear and rotationality driven by the nonlinear wave traveling up the steep slope may be important to the wave kinematics in this region. Due to this inconsistency of expectations in the vertical velocity component, the orientation of the ADV was rechecked and the instrument reinstalled multiple times, but it always yielded the same results. Sophisticated three-dimensional numerical simulations (Higuera et al. 2013) are unable to reproduce this negative vertical velocity (although available supercomputer computational resources may not have allowed a cell resolution sufficient to resolve the boundary layer), and thus there is the possibility that it is a relic of measurement error or instrument interference.

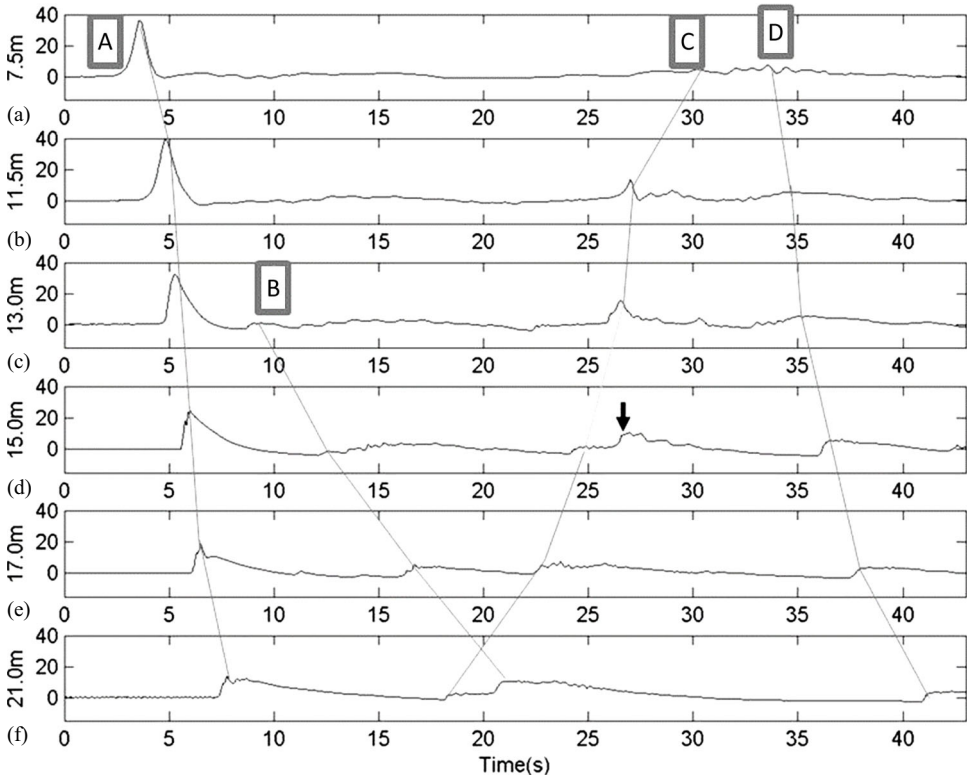

Fig. 7. rWG free surface elevation (cm) over time of several rWGs located along the centerline of the basin ($Y = 0$ m), where the X positions are given by the labels for each vertical axis. Gray lines show identified bore fronts: (a) generated wave; (b) secondary bore front; (c) reflected bore front; and (d) return wave/bore front, and times they pass each rWG. Arrow denotes localized event.

J. Waterway, Port, Coastal, Ocean Eng., 2019, 145(6): 04019024

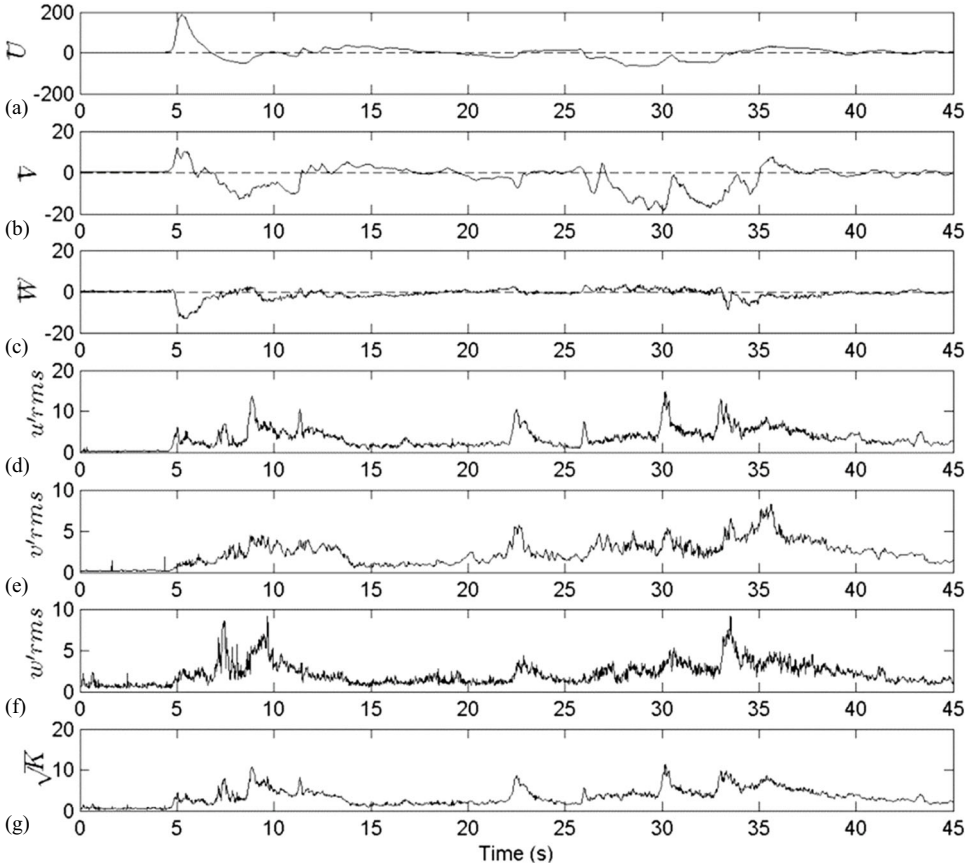

Fig. 8. (a–c) Mean velocities; (d–f) RMS turbulent fluctuations; and (g) square root of turbulent kinetic energy at the apex of the shelf ($X = 13$ m, $Y = 0$ m, $Z = 0.75$ m); all units in cm/s.

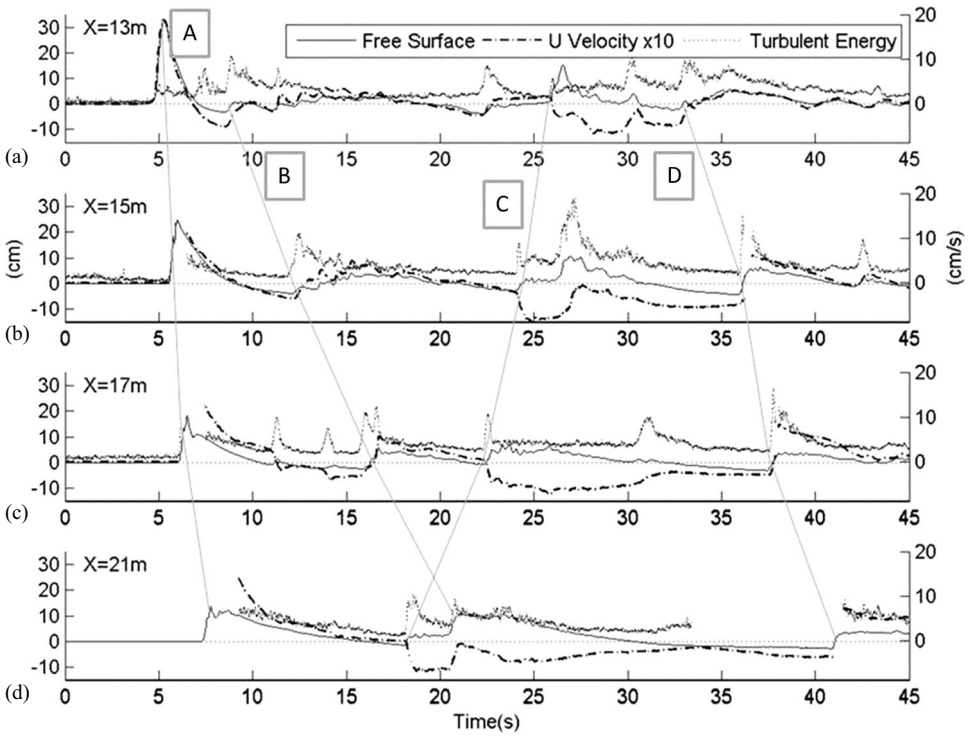

Fig. 9. Free surface (cm, following the left vertical axis), mean velocity × 10 (cm/s, following the right vertical axis), and square root of K (cm/s, following the right vertical axis) of ADV colocated with rWG positioned on the shelf and along centerline at $Y = 0$ m and X positions given in each subplot.

J. Waterway, Port, Coastal, Ocean Eng., 2019, 145(6): 04019024

RMS fluctuations show numerous isolated events or peaks in magnitude. These events correspond to changes in the mean flow directions from at least one the components and are comparable in magnitude across all three velocity components. Fig. 8 provides some guidance to compare the magnitude of turbulence generated by bottom friction to the turbulence generated at the free surface by the turbulent, breaking bore fronts. From 15 to 20 s, the flow near the apex can be characterized as slowly varying onshore-directed flow with noticeable transitions; turbulent energy during this interval is low and steady. We can compare this steady period to a time influenced by the passage of bore fronts. At 35 s, the flow is comparable in magnitude in the mean sense to the flow at 15–20 s, but is immediately after Bore Front D passes. Through comparing these two different times, we see that the square root of the turbulent kinetic energy, $\sqrt{K}$, which corresponds with the bore front passing ($\sim$35 s), is 6–10 times larger than the square root of the turbulent kinetic energy driven by bottom stress during quasi-steady flow (15–20 s).

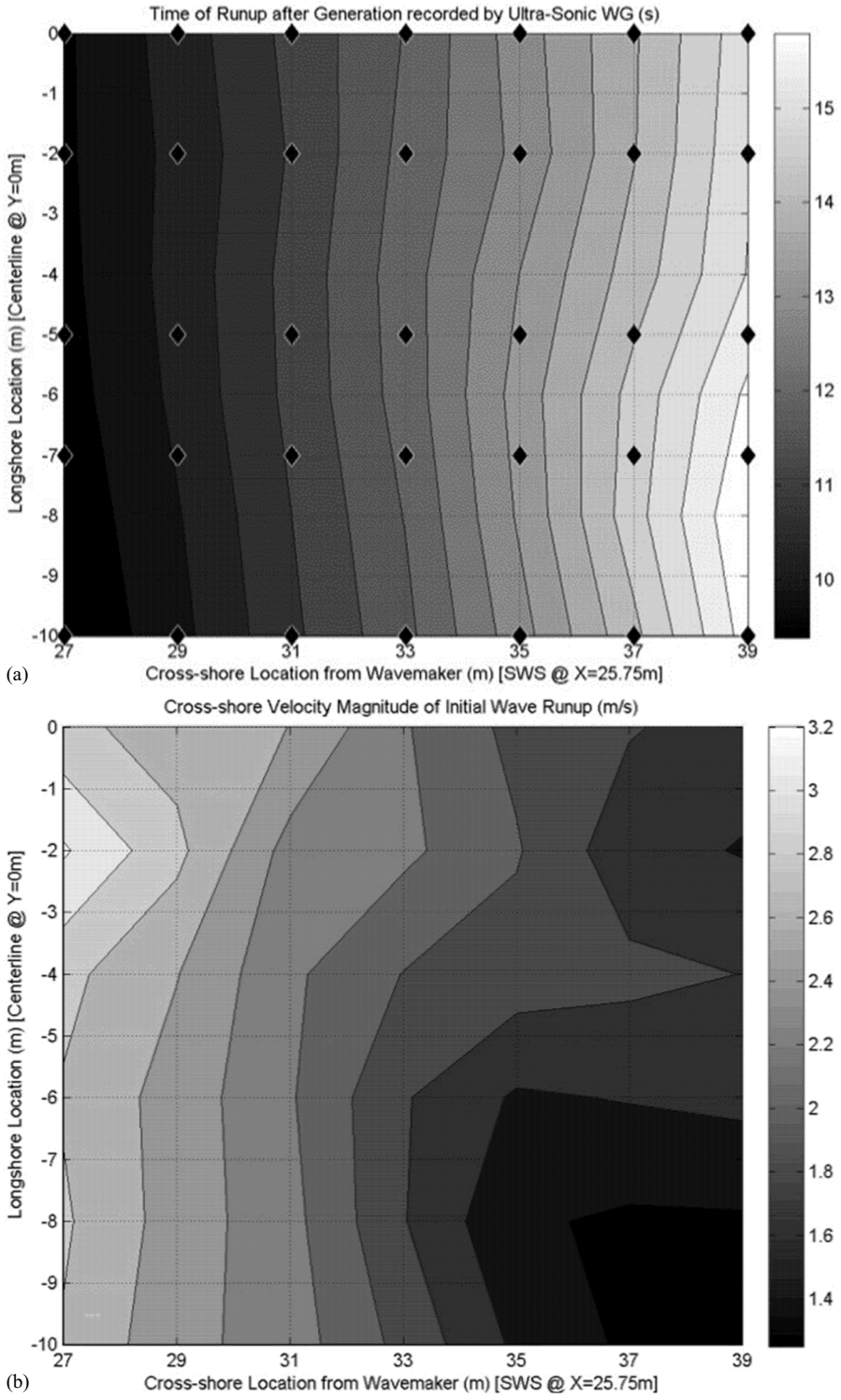

Fig. 10. (a) Arrival time in seconds, as recorded by the usWG, of the solitary wave bore front on the planar beach shoreward of the SWS, where black diamonds represent usWG locations; and (b) U component of the bore front velocity above the SWS on the planar beach as recorded by the usWG.

J. Waterway, Port, Coastal, Ocean Eng., 2019, 145(6): 04019024

In an attempt to summarize the measured free surface and turbulence data and correlate the bore front features with these measurements, Fig. 9 presents information at four different locations. The locations presented are on the shelf along the centerline where ADVs were colocated with the four most-onshore rWG locations. In the figure, the intermittent times where turbulence data are not presented were due to air entrainment or exposed (nonsubmerged) ADVs. At each location, the passing of the four bore fronts defined previously can be identified by gray lines representing Bore Fronts A–D. At the time a bore front passed each measurement location, there was an increase in turbulent energy and a change in the fluid velocity with time. The converging waves that collided near the apex after Bore Front C as discussed in Fig. 5(e) could be identified in the time series at $X = 13$ m around 30.5 s, at $X = 15$ m around 27 s, and at $X = 17$ m around 31 s by the spikes in turbulent energy and acceleration of the fluid.

Uprush on Planar Beach

With the basin hydrodynamics and evolution of the solitary wave over the SWS previously described, the next focus is on the planar beach shoreward of the SWS. By tracking the arrival time of Bore Front A using the usWGs, the velocity of this bore front in the cross-shore direction (U component) could be found. Fig. 10 shows Bore Front A arrival times along the top of the plot. The contour line variations suggest that the wave front was not uniform along the shore during the uprush. For example, the bore front at $X = 29$ m arrived first near the sidewall of the basin ($Y \approx -10$ m). The lag in the arrival time at $X = 29$ m along the centerline of the basin was observed to be the result of the wave traveling over the widest section of the shelf. The wave travels a longer distance in shallower water, which slows down propagation. Once the wave uprush has reached $X = 39$ m, the initial alongshore orientation had inverted.

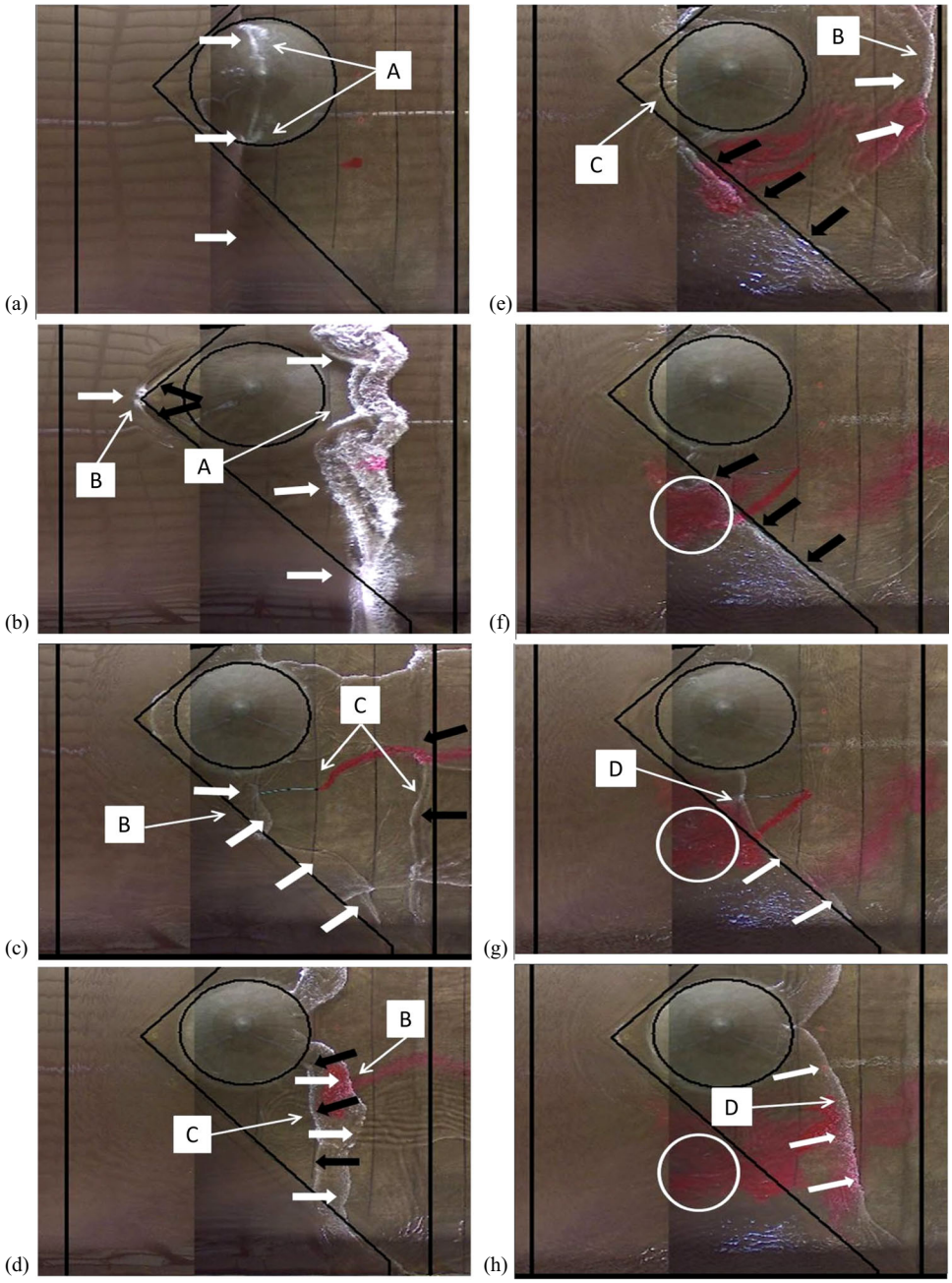

Fig. 11. Basin at (a) 6.2 s; (b) 8 s; (c) 15 s; (d) 20 s; (e) 27.4 s; (f) 32.3 s; (g) 39.3 s; and (h) 42.2 s after the solitary wave was generated. Arrows indicate mean flow direction, with white arrows indicating onshore flows and black arrows indicating offshore flows.

J. Waterway, Port, Coastal, Ocean Eng., 2019, 145(6): 04019024

The bore front arrived near the centerline of the basin first and near the wall of the basin last.

To estimate the cross-shore velocity, uprush arrival times were differenced with respect to the known location of the usWG. The data revealed that the lowest uprush velocity occurred at $X = 39$ m near the sidewall of the basin, while the highest uprush velocity occurred at $X = 27$ m near the centerline of the basin. The highest uprush velocity occurred because of a jetting mechanism generated by wave energy refracting along the shelf, focusing the energy toward the centerline. The jetting caused the velocity to initially focus near the centerline and eventually spread laterally with time at each sequential cross-shore location. Lateral variations in the bore front velocity magnitude were between 10% and 30%. Therefore, the shape and velocity of the uprush were weakly influenced by the alongshore variability of the bathymetry offshore of the SWS.

Triangular-Shaped Shelf with Conical Island

In this section, we will concisely present the second experiment. As mentioned previously, the second experiment was a modification of the first, in that a conical island with base radius of 3.0 m was placed along the centerline of the shelf. This section will describe the hydrodynamics observed, and is followed by detailed discussions of the differences found between the first (no-island) and second (with-island) experiments. Plan view images of the southern half of the basin for the with-island experiment are presented in Fig. 11. The lines drawn on the images have the same definitions as in the previous experiment. The black circle represents approximately the submerged perimeter of the island, and the V-shaped diagonal black lines delineate the shelf edge. For flow visualization, dye was injected into the water from a continuous point source behind (on the onshore side) of the island.

The solitary wave arrives at the apex of the shelf at time 6.2 s, overtops the island, and then begins to break on the sides of the island as shown in Fig. 11(a). The dense localized white areas appearing on the back side of the island are associated with the leading wave and are labeled Bore Front A. The onshore flow associated with Bore Front A is indicated with white arrows. Multiple wave fronts were generated at the back of the island at 8 s and then extended to the side walls of the basin as shown in Fig. 11(b). The flow direction behind Bore Front A was still on shore (white arrows), while the flow direction at the offshore end of the shelf was off shore (black arrows), similar to the no-island experiment. The effect of the island on the alongshore profile of Bore Front A is evident, with clear amplification of the bore front at Y locations equal to $\pm$ the island radius. The dye release started before the arrival of Bore Front A and it was well mixed by the breaking bore and advected by the onshore flow. At the shelf apex, a sill-type bore front was generated and is labeled Bore Front B. Bore Front B propagated along the shelf edge and toward the shallow water shelf with onshore flow as indicated by the white arrows shown in Fig. 11(c) at 15 s.

Different from the no-island experiment, Bore Front C consisted of the combined flow reflected off the SWS (as in the no-island experiment) as well as the flow reflected off the island. Both Bore Fronts B and C appear in Fig. 11(d) after passing through each other at time 20 s. The interaction of Bore Fronts B and C caused strong mixing and horizontal dispersion of the dye. At 27.4 s, Bore Front B continued to travel on shore but with significant front curvature, and Bore Front C traveled around the island and converged at the shelf apex as shown in Fig. 11(e). The dye was transported off shore of the shelf edge by the flow shown with the black arrows. The apex

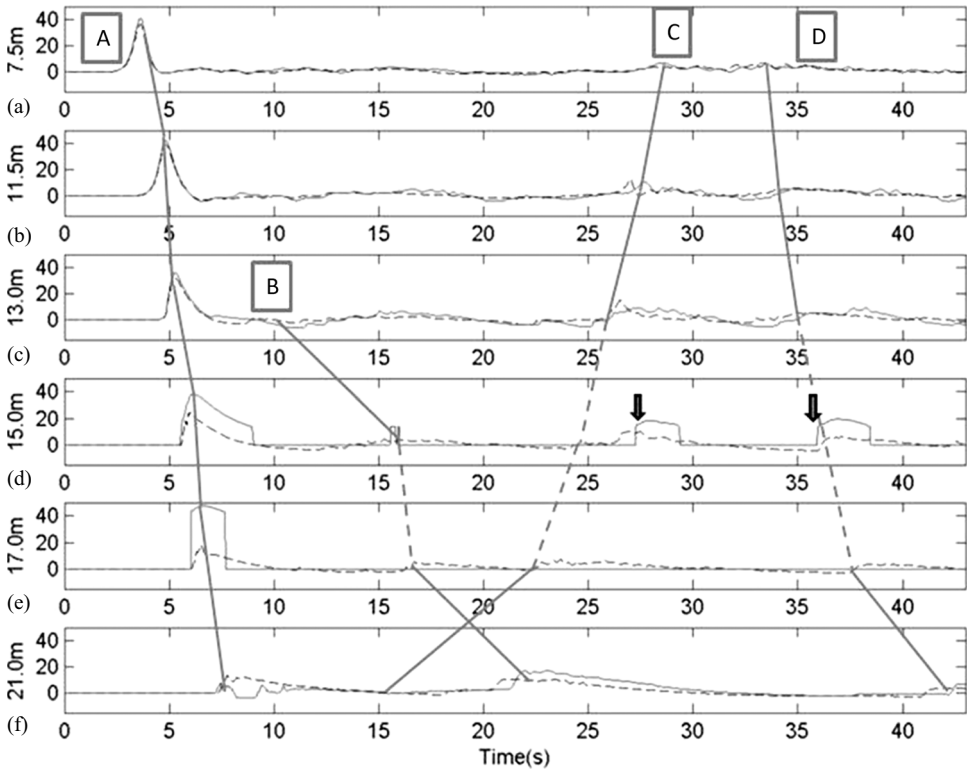

Fig. 12. rWG free surface elevation (cm) over time of several rWGs located along the centerline of the basin ($Y = 0$ m). Gray lines show identified bore fronts: (a) generated wave; (b) secondary bore front; (c) reflected bore front; and (d) return wave/bore front, and times they pass each rWG. Arrows denote localized events; solid lines denote triangular shelf with island experiment; and dashed lines denote triangular shelf experiment.

J. Waterway, Port, Coastal, Ocean Eng., 2019, 145(6): 04019024

convergence in this experiment appears more energetic as compared to the no-island experiment, and it will be discussed subsequently.

As with the no-island experiment, a stationary hydraulic jump formed along the shelf edge following the passage of Bore Front C. This process led to strong mixing along the shelf break as is evident in Fig. 11(f), indicated by the spreading of dye over a wide offshore area. It is in this mixing area that an eddy, very similar to that found in the no-island case, exists. The eddy persisted for more than 5 s because it is still clearly visible in Fig. 11(g). Near 39 s, another sill-type Bore Front C arrived on the shelf and traveled onshore. The onshore flow associated with this bore front is shown by the white arrows in Fig. 11(h). By 42.2 s [Fig. 11(h)], Bore Front D propagated further landward and traveled around the island, causing the flow over the shelf to be directed on shore.

Discussion and Comparison between Experimental Configurations

Here, we highlight the differences found in the no-island (first) and with-island (second) experiments, examining measurements in free surface elevation, velocity, and turbulence. A comparison of the surface elevation recorded from rWGs along the basin centerline for the two experiment sets is presented first. rWGs along $Y = 0$ m for the two experiments are given in Fig. 12 for $X = 7.5$, 11.5, 13.0, 15.0, 17.0, and 21.0 m. The layout of this figure is the same as that of Fig. 8, but with data from both experiments. Gauge locations of $X = 15.0$ m and $X = 17.0$ m are situated above the island; both are initially dry.

What is immediately obvious is that, off shore of the island ($X = 7.5$, 11.5, and 13.0 m), the effect of the island on the free surface elevation time series is weak. There are subtle differences in the wave field at later times, but the magnitude of these differences is small compared to the elevation of the leading wave. As expected, in the immediate vicinity of the island ($X = 15.0$ and 17.0 m), the elevation differences are substantial, owing of course to the run-up of the wave on the island slope. In the second experiment, it is noticed that there are two events (black arrows) at $X = 15.0$ m. These two events are the result of the strong convergence at the apex and the reflected and refracted flow in the front of the island. The dashed line represents the imaginary locations of the bore fronts if the island was not there and are provided only for a visual aid. Behind the island, at $X = 21.0$ m, the differences in elevations are still relatively large. The leading Bore Front A has an amplitude 50%

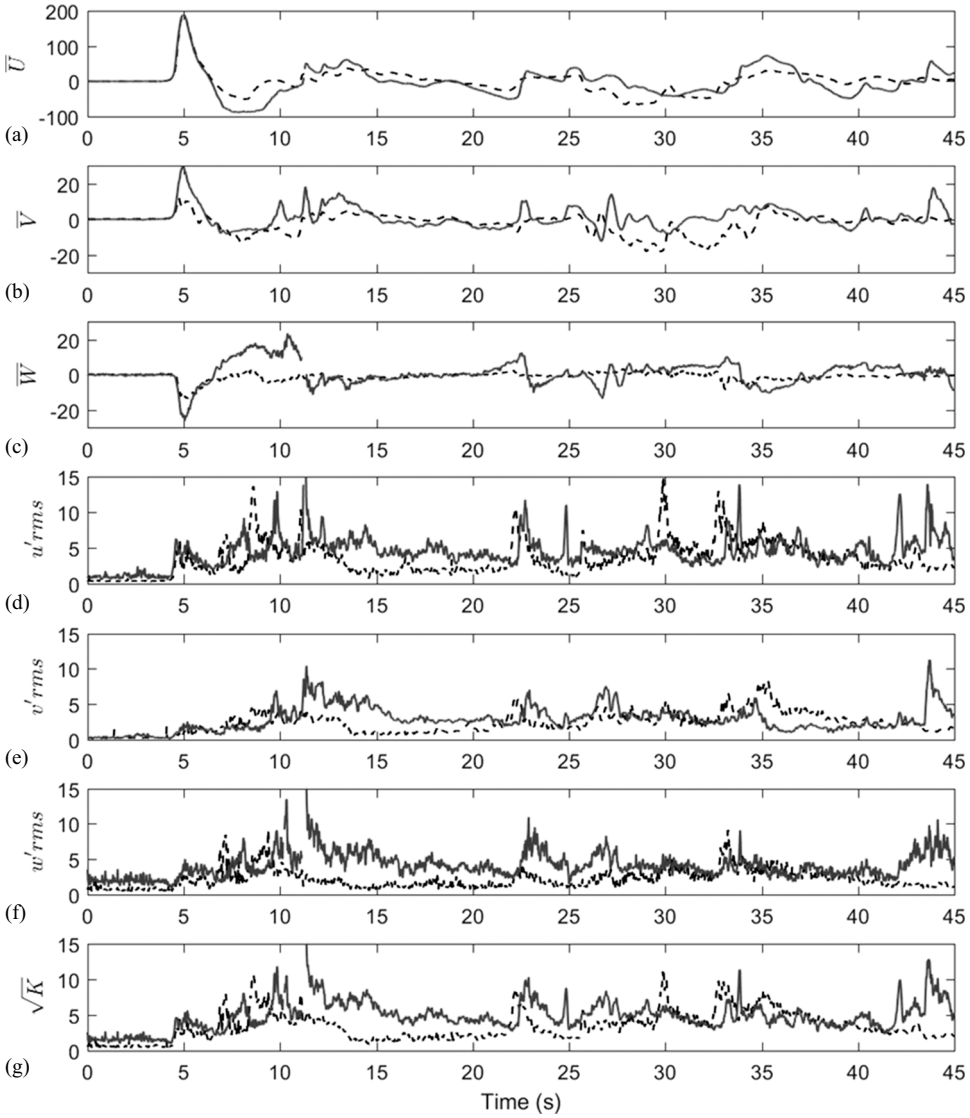

Fig. 13. (a–c) Mean velocities; (d–f) RMS turbulent fluctuations; and (g) square root of turbulent kinetic energy at the apex of the shelf ($X = 13$ m, $Y = 0$ m, $Z = 0.75$ m); all units in cm/s. Dashed lines indicate triangular shelf experiment; solid lines indicate triangular shelf with island experiment.

J. Waterway, Port, Coastal, Ocean Eng., 2019, 145(6): 04019024

less with the island in place, while Bore Front B has an amplitude 50% greater with the island. The with-island height decrease in the relatively fast-moving Bore Front A is due to the wake-like shadowing effect of the island, while the increase in the relatively slow-moving Bore Front B is due to a refractive convergence of the wave in the lee of the island. While both Bore Fronts A and B have similar propagation directions, the large difference in bore speeds (i.e., Froude numbers), leads to different processes controlling the flow field behind the island. While not shown here, another comparison of the measured surface elevation was carried out for the two experiment sets at different locations in the alongshore direction on the shelf, at $Y = 1$, 2, and 5 m. At $Y = 5$ m, there is a small difference in the surface elevation between the two experiment sets on the shelf, with differences similar to those observed at ($X = 11.5$ m, $Y = 0$ m) in Fig. 11; this indicates that the lateral effect of the island on the measured on-shelf surface elevations diminishes within one diameter distance from the center of the island.

Next, the effects of the island on turbulence characteristics were investigated by comparing turbulence intensities and transport. The comparison of the three velocity components of the mean flow, their RMS turbulent fluctuations, and turbulent kinetic energy K at the apex of the shelf are shown in Fig. 13. The mean flow velocity comparisons are shown in Figs. 13(a–c). In both experiments, the horizontal mean velocity $\overline{U}$ is the dominant velocity component, with peak speed of nearly 2 m/s. The negative velocity trough in $\overline{U}$ found near 8 s is larger in the second experiment due to the stronger

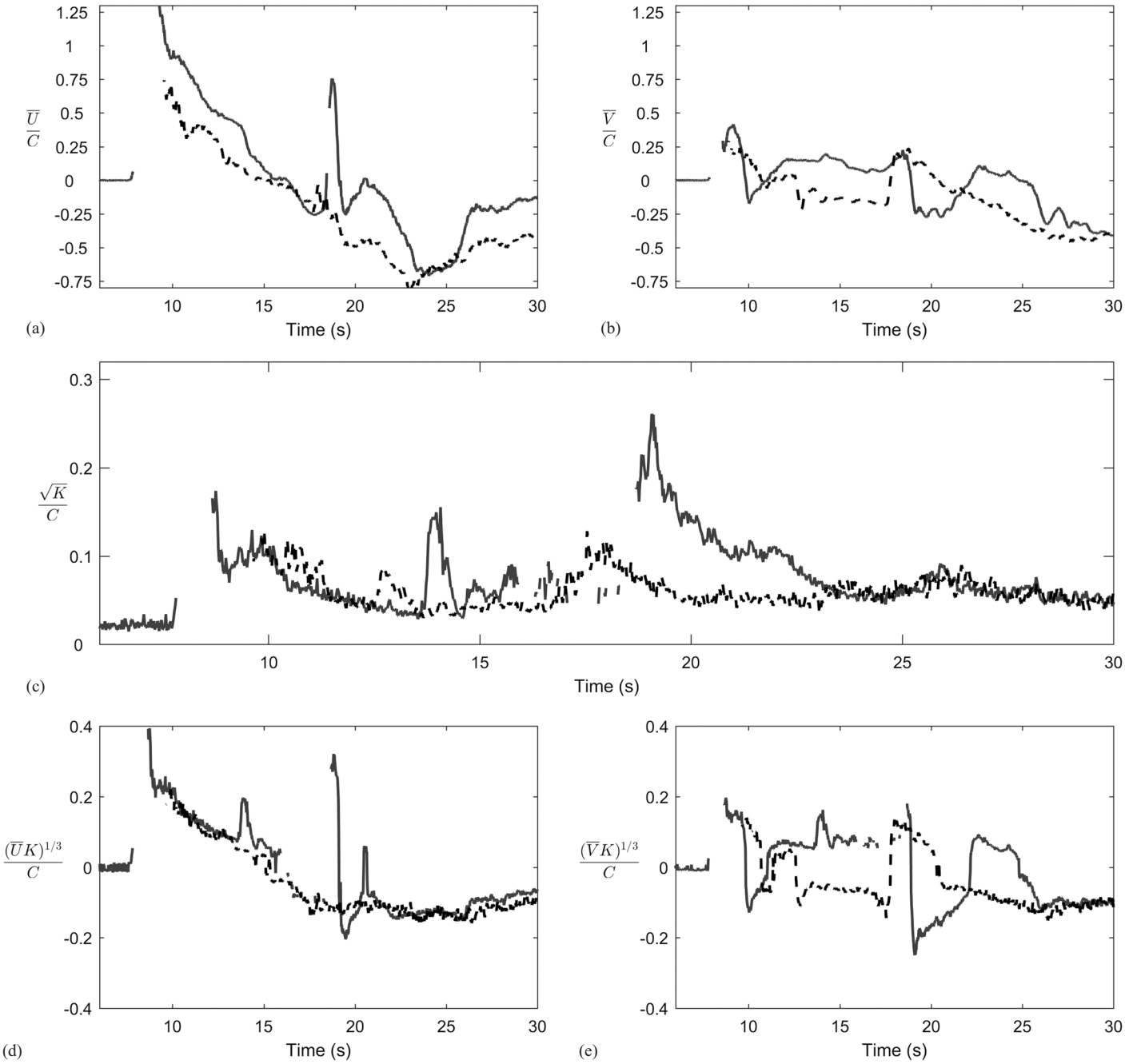

Fig. 14. (a–b) Mean velocity components; (c) turbulent kinetic energy; and (d–e) turbulent transport at $X = 21$ m, $Y = -2$ m, and $Z = 0.77$ m; still-water depth at this location is 6.3 cm ($C = 78.6$ cm/s). Dashed lines indicate triangular shelf experiment; solid lines indicate triangular shelf with island experiment.

J. Waterway, Port, Coastal, Ocean Eng., 2019, 145(6): 04019024

reflection off the island. The peak horizontal mean velocity in $\overline{V}$ at 5 s is larger in the second experiment, as is the vertical mean velocity, $\overline{W}$. There is no immediately obvious physical reason for this increase, particularly because this ADV measurement volume was located along the centerline of a symmetrical configuration. Although the instrument was repeatedly checked, the increase may indicate an alignment error and/or a lack of precise symmetry in the bathymetry configuration, with increased $\overline{V}$ and $\overline{W}$ magnitudes in the island experiment possibly due to the flow divergence around the island.

The comparison of the turbulent fluctuations are shown in Figs. 13(d–f). In general, for the first 7 s of the experiments, covering the passage of the solitary wave, the two experiments provide similar turbulence levels. After this time, the turbulence behavior between the two experiments appears weakly correlated in both magnitude and time, with the island experiment showing a clearly larger turbulent energy in all directions from 10 to 30 s. This jump in turbulence from 10 to 30 s is clearly evident in the turbulent kinetic energy, K, plotted in Fig. 13(g). During this time, $K^{1/2}$ is 25%–80% larger in the with-island experiment, and from 15 to 20 s in the with-island experiment, $K^{1/2}$ is the same order as the mean speed. This additional turbulence is primarily due to the offshore-directed run-down flow coming from the island.

While the data in Fig. 13 provide a description of the flow in front of the island, it is behind the island where the effects are strongest. The ADV at location $X = 21$ m and $Y = -2$ m was chosen to analyze turbulence behaviors for the two experiment sets. Here, we will examine normalized flow properties and present turbulent flux quantities (i.e., Ting and Kirby 1995). All velocities were normalized by the wave celerity $C = (gh)^{1/2}$, where h is the local still-water depth. The mean velocity, the turbulent kinetic energy, and the energy flux at $X = 21$ m and $Y = -2$ m are shown in Fig. 14.

Fig. 14(a) shows that the magnitude of the mean velocity in the x-direction, $\overline{U}$, is quite similar for the two experiments, with the largest differences occurring well after the passage of the leading wave. On the other hand, the mean velocity in the y-direction, $\overline{V}$, shows substantial differences across the two experiments, as shown in Fig. 14(b). In the no-island experiment, $\overline{V}$ is expectedly near zero for the leading wave because there is only minor alongshore variation in the front. Due to the presence of the island in the second experiment, the wave front has a strong $+Y$ motion (at $Y = -2$ m) because the energy attempts to fill the shadowed area behind the island. During the passage of the leading wave, the total speed of the fluid is larger in the with-island experiment at this location.

Comparison of the scaled square root of turbulent kinetic energy is given in Fig. 14(c). The turbulent energy decays rapidly after the passage of the leading Bore Front A at time 8–13 s for both experiments. Afterward, in the time frame from 13 to 17 s, the turbulent energy remains low for the first experiment, while there are numerous large peaks and generally greater turbulence in the with-island experiment. This greater turbulence in the second experiment arises from the run-down flow off the island, advected away from the island by the mean flow. The turbulence peak at ~ 18 s in both experiments is due to the interaction of wave Bore Front B and wave Bore Front C. We suppose the larger turbulence peak in the second experiment is due to the preexisting higher turbulence level before the bore collision. After this event at ~ 18 s, the turbulence level is highly similar between the two experiments, indicating the effect of the island on this quantity is weak at later times.

Turbulent energy flux comparisons are shown in Figs. 14(d and e). In both experiments, the turbulence transport in the x-direction by the mean flow [Fig. 14(d)] is in the onshore direction until ~ 18 s, when the transport shifts to off shore. The turbulence transport is higher in

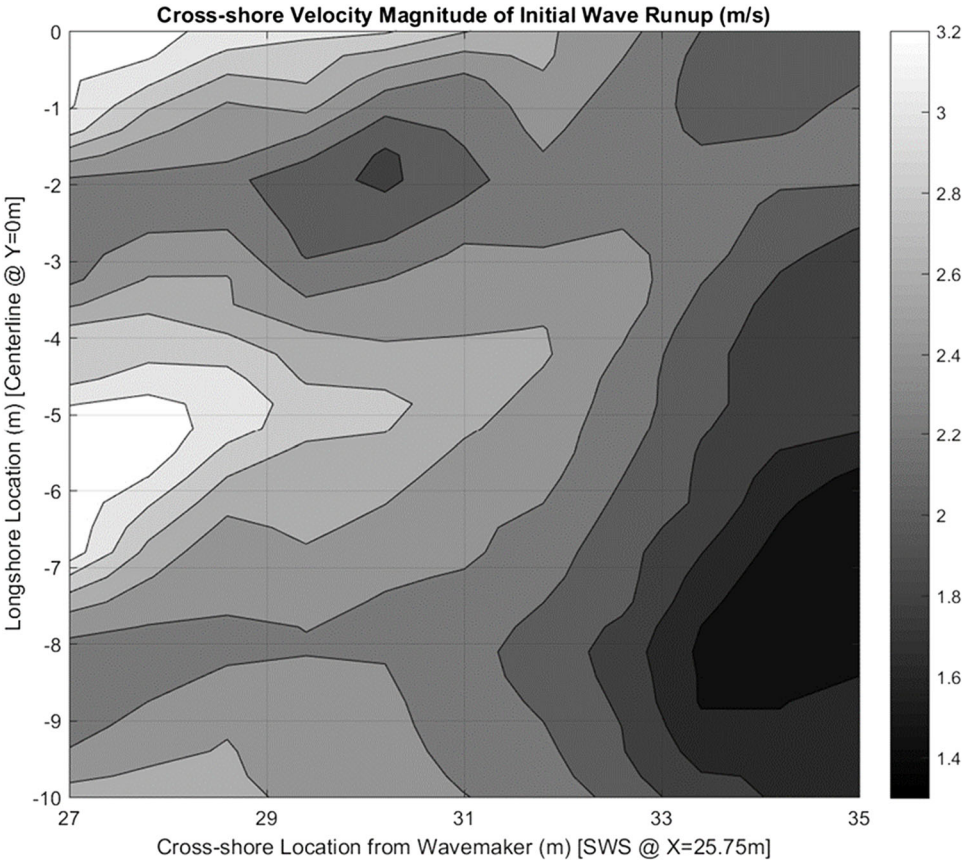

Fig. 15. U component of the bore front velocity above the SWS on the planar beach as recorded by the usWG for the with-island configuration.

J. Waterway, Port, Coastal, Ocean Eng., 2019, 145(6): 04019024

the second experiment, in agreement with the observed higher turbulent kinetic energy. The turbulence transport in the y-direction by the mean flow is almost negligible for the first experiment as shown in Fig. 14(e), while this longshore transport in the second experiment has a magnitude equal to the x-direction transport. Locally, the island causes leading order changes to $\overline{V}$, the turbulent kinetic energy, and the turbulent flux, but these changes are largely restricted to early times, during the passage of the leading wave.

The usWGs on the planar beach are used to track the leading bore front as it travels up the beach, using the same procedure as described for the no-island experiment. Fig. 15 shows the contours of the cross-shore velocity magnitude. The velocity magnitude is strongly nonuniform in the alongshore direction near the SWS ($X = 27$ m), and this nonuniformity lessens as the bore travels up the beach. The greatest uprush velocity occurs between $X = 27$ m and $X = 29$ m in two locations: near the basin centerline and around $Y = 5-6$ m. The higher velocity along the basin centerline is due to the same jetting mechanism and wave refraction process found in the no-island experiment, although enhanced here by the island shadowing effect. The highest velocity in this case is larger by approximately 20% compared to the no-island experiment.

Conclusion

The experimental study discussed here investigated the evolution of a breaking solitary wave propagating over (1) a shallow water shelf, and (2) a shallow shelf with a conical island. Near the shelf break, the breaking solitary wave could be characterized as a plunging breaker. In both experiments, the interaction of the solitary wave and the bathymetry led to the development of four separate wave events, characterized as bore fronts, that each propagated across the shallow shelf. In addition, in the second experiment the solitary wave energetically overtopped the island. The hydrodynamics on the shelf and around the island are clearly more complex, with higher turbulence levels near the island.

The solitary wave transformation was recorded on shore and off shore of the SWS with free surface elevation measurements. In both experiments, minimal wave shoaling was observed at the apex as the wave propagated over the shelf. Shoaling was observed along the milder slopes near the basin side walls. In the first experiment, once the wave traveled over the shelf edge, the wave height rapidly decayed on shore because of breaking. In the second experiment, the island induced greater dissipation through turbulence, but also had a significant effect on the alongshore distribution of energy, leading to localized hot spots of high current and turbulence.

Once the solitary wave propagated over the shelf to the SWS, the flow over the planar beach was not uniform (in the alongshore direction). Here, variations were driven by the shelf bathymetry. Closest to the SWS, the wave arrived near the sidewall of the basin first. Further up the initially dry beach, the wave arrived near the centerline of the basin in both experiments first. However, the specific patterns of the front arrival time and the associated front speed were quite different between the two experiments. In the no-island experiments, the speeds were relatively regular and readily explained via a refractive focusing of wave energy toward the centerline of the basin. On the other hand, in the second experiment the front speeds showed very high alongshore variability, including a clear high front speed region located one island diameter from the centerline.

During both experiments, a total of four bores, including the bore front from the incident solitary wave, were tracked using both the measured free surface elevation and the fluid velocity data. The largest turbulent events in the record corresponded to the passing bore fronts. This result suggests that horizontal shear and wave breaking play a significant role in turbulence generation on the shelf. The effect of the conical island on the measured surface elevation appears to diminish within one diameter distance from the island center. The higher turbulence intensity observed in the second experiment indicates an increase in the mixing rate due to the strong convergence of the flow around the island as well as the breaking along its edges. Off shore from the shelf, a three-dimensional coherent turbulent structure developed once Bore Front C propagated off shore.

The data and discussion presented in this paper provide insight into long-wave propagation and evolution over shallow bathymetry. In addition, the experiment could also be used as a three-dimensional data set to calibrate and validate numerical models (e.g., Lynett et al. 2017). While extrapolating to geophysical-scale events should be done with caution, a few conclusions from the experimental results can be made. First, while it is generally accepted that long-wave runup is primarily driven by the upper beach slope (e.g., Synolakis 1987), results from this experiment indicate that shallow water offshore bathymetry also influences wave inundation. However, for this role to be significant (i.e., leading order), the bathymetry variability needs to be strong and local, such as that found for the island experiments, near to the island. When considering strongly turbulent processes, such as transport and mixing, the experimental results suggest that bore-front-generated turbulence and associated gradients in spatial velocity dwarfs the turbulence generated by bottom stress. Finally, abrupt variations in nearshore bathymetry can lead to unstable mixing regions that are capable of shedding persistent eddies, which in turn can cause localized mixing and transport.

Data Availability Statement

The data presented in this paper were used as part of a workshop benchmarking exercise, and are archived at the workshop website (http://isec.nacse.org/workshop/2009_isec/). Furthermore, the complete experimental data set, including all raw data, is archived at the DesignSafe-CI Data Depot (https://www.designsafe-ci.org/).

References

Gedik, N., E. Irtem, and S. Kabdasli. 2005. "Laboratory investigation on tsunami run-up." *Ocean Eng.* 32 (5–6): 513–528. https://doi.org/10.1016/j.oceaneng.2004.10.013.

Grilli, S. T., R. Subramanya, J. T. Kirby, and G. Wei. 1994a. "Comparison of modified Boussinesq and fully nonlinear potential models for shoaling solitary waves." In *Proceedings of the international symposium on waves: physical and numerical modeling*, edited by R. Isaacson and R. Quick, 524–533. Vancouver: University of British Columbia.

Grilli, S. T., R. Subramanya, I. A. Svendsen, and J. Veeramony. 1994b. "Shoaling of solitary waves on plane beaches." *J. Waterway, Port, Coastal, Ocean Eng.* 120 (6): 609–628. https://doi.org/10.1061/(ASCE)0733-950X(1994)120:6(609).

Higuera, P., J. L. Lara, and I. J. Losada. 2013. "Simulating coastal engineering processes with OpenFOAM." *Coastal Eng.* 71: 119–134. https://doi.org/10.1016/j.coastaleng.2012.06.002.

Hsiao, S. C., T. W. Hsu, T. C. Lin, and Y. H. Chang. 2008. "On the evolution and run-up of breaking solitary waves on a mild sloping beach." *Coastal Eng.* 55 (12): 975–988. https://doi.org/10.1016/j.coastaleng.2008.03.002.

Lin, C., and H. H. Hwung. 1992. "External and internal flow fields of plunging breakers." *Exp. Fluids* 12–12 (4–5): 229–237. https://doi.org/10.1007/BF00187300.

Liu, P. L.-F., and K. Al-Banaa. 2004. "Solitary wave runup and force on a vertical barrier." *J. Fluid Mech.* 505: 225–233. https://doi.org/10.1017/S0022112004008547.

Liu, P. L.-F., Y. Cho, M. J. Briggs, U. Kanoglu, and C. E. Synolakis. 1995. "Runup of solitary waves on a circular Island." *J. Fluid Mech.* 302: 259–285. https://doi.org/10.1017/S0022112095004095.

Liu, P. L.-F., C. E. Synolakis, and H. H. Yeh. 1991. "Report on the international workshop on long-wave run-up." *J. Fluid Mech.* 229 (1): 675–688. https://doi.org/10.1017/S0022112091003221.

Lynett, P., and P. L.-F. Liu. 2004. "A two-layer approach to wave modeling." *Proc. R. Soc. London Ser. A* 460 (2049): 2637–2669. https://doi.org/10.1098/rspa.2004.1305.

Lynett, P. J., et al. 2017. "Inter-model analysis of tsunami-induced coastal currents." *Ocean Model.* 114: 14–32. https://doi.org/10.1016/j.ocemod.2017.04.003.

Lynett, P. J., D. Swigler, S. Son, D. Bryant, and S. Socolofsky. 2011. "Experimental study of solitary wave evolution over a 3D shallow shelf." *Int. Conf. Coastal. Eng.* 1 (32): 1. https://doi.org/10.9753/icce.v32.currents.1.

Madsen, P. A., D. R. Fuhrman, and H. A. Schäffer. 2008. "On the solitary wave paradigm for tsunamis." *J. Geophys. Res.* 113 (C12). https://doi.org/10.1029/2008JC004932.

Monaghan, J. J., and A. Kos. 1999. "Solitary waves on a Cretan beach." *J. Waterway, Port, Coastal, Ocean Eng.* 125 (3): 145–155. https://doi.org/10.1061/(ASCE)0733-950X(1999)125:3(145).

Synolakis, C. E. 1987. "The runup of solitary waves." *J. Fluid Mech.* 185: 523–545. https://doi.org/10.1017/S002211208700329X.

Ting, F. C. K. 2006. "Large-scale turbulence under a solitary wave." *Coastal Eng.* 53 (5–6): 441–462. https://doi.org/10.1016/j.coastaleng.2005.11.004.

Ting, F. C. K., and J. T. Kirby. 1994. "Observation of undertow and turbulence in a laboratory surf zone." *Coastal Eng.* 24 (1–2): 51–80. https://doi.org/10.1016/0378-3839(94)90026-4.

Ting, F. C. K., and J. T. Kirby. 1995. "Dynamics of surf-zone turbulence in a strong plunging breaker." *Coastal Eng.* 24 (3–4): 177–204. https://doi.org/10.1016/0378-3839(94)00036-W.